Applied Materials Today 42 (2025) 102573

Contents lists available at ScienceDirect

Applied Materials Today

journal homepage: www.elsevier.com/locate/apmt

Hydrophobic post-functionalization of a water instable bioMOF: Effect on CO_2 and water adsorption

Albert Rosado [a,*], Alejandro Borrás [a], Fabián Suárez-García [b], Oriol Vallcorba [c], Ana M. López-Periago [a], José A. Ayllón [d,*], Concepción Domingo [a,*]

[a] Materials Science Institute of Barcelona (ICMAB-CSIC), Campus UAB s/n, 08193 Bellaterra, Spain
[b] Instituto de Ciencia y Tecnología del Carbono (INCAR-CSIC), C/ Francisco Pintado Fe, 26, 33011 Oviedo, Spain
[c] ALBA Synchrotron Light Source, 08290 Cerdanyola del Vallés, Spain
[d] Departament de Química, Universitat Autònoma de Barcelona (UAB), Campus UAB s/n, 08193 Bellaterra, Spain

ARTICLE INFO

Keywords:
BioMOF
Hydrophobicity
Aerogel
Gas adsorption
Green chemistry

ABSTRACT

The preparation of highly porous metal organic frameworks (MOFs) chemically resistant to water is essential for the forthcoming use of these materials as adsorbents in applications of gas separation under moisture or for wastewater remediation. However, most of the synthesized MOFs have a framework with low thermodynamic stability against water. MOFs modification performed in this work aims to modify the water behavior by addressing kinetic factors affecting the dissolution reaction rate. For this purpose, a post-synthetic process is designed to functionalize MOF particles on the surface with a hydrophobic compound, particularly, stearic acid. The microporous bioMOF CaSyr-1, recently synthesized in our laboratories, was selected as a case study. Pristine CaSyr-1 transforms in water into a second crystalline phase, CaSyr-2 with a non-porous structure resolved in this work. An external surface coating method was chosen to prevent the bioMOF from water-induced degradation, while preserving the internal empty volume to a large extent, thus almost not affecting the adsorption capacity. The developed synthetic method allows the straightforward assembly of the composite CaSyr-1/stearate into a monolithic aerogel with a multimodal porosity. The significant enhancement of the kinetic stability of the hydrophobized CaSyr-1 with respect to the parent bioMOF was demonstrated by structural and morphological analysis. Textural properties and adsorption capacities of CaSyr-1/stearate were evaluated with different adsorbates, including N_2, CO_2 and H_2O. In particular, significant water adsorption was attained in the coated MOF without affecting the integrity of the framework. Besides, water adsorption works as an effective activation method for the composite by displacing stearic acid adsorbed inside CaSyr-1 pores. As a consequence, CO_2 adsorption at room temperature in the water-activated sample was enhanced by a factor of two with respect to the vacuum-activated sample, reaching and uptake of 31 cm^3 of CO_2 per gram of adsorbent.

1. Introduction

Metal organic frameworks (MOFs) are crystalline materials, assembled through coordination bonds established between metal ions or clusters and polytopic organic linkers, with an open framework containing potential voids permeable to fluids [1]. In the vast arena of porous matter, MOFs offer unprecedented versatile chemistry, since they can be constructed from a wide variety of inorganic building units and organic linkers, presenting pore sizes in the micro and meso ranges, as well as rigid or flexible frameworks [2]. In addition, their exceptionally high pore volume and specific surface area extend the use of MOFs to a wide range of domains, such as adsorption, catalysis or biomedicine [3]. In particular, global climate change, driven by the increase in atmospheric carbon dioxide (CO_2) levels, is one of the greatest challenges our planet is facing today. Considering that the field of MOF research is exceptionally diverse, a significant number of this porous materials have already been suggested for CO_2 capture and separation. Despite the constant increase of newly synthesized MOFs, only few of them are water-stable and can be applied in realistic conditions of CO_2 adsorption, *e.g.*, under moisture, or in wastewater remediation [4–7].Hence, the preparation of highly porous MOFs chemically resistant to moisture or water is considered essential. Many

---

* Corresponding authors.
E-mail addresses: arosado@icmab.es (A. Rosado), JoseAntonio.Ayllon@uab.es (J.A. Ayllón), conchi@icmab.es (C. Domingo).

https://doi.org/10.1016/j.apmt.2024.102573
Received 1 October 2024; Received in revised form 5 December 2024; Accepted 23 December 2024

highly porous MOFs comprising divalent metals and carboxylates, which are some of the most easily synthesized MOFs [8], are usually unstable in aqueous solutions or even in humid air, since the involved carboxylate-M^{2+} bonds are weak and can be easily replaced by coordinating water molecules [9]. This substitution leads, in most cases, to the collapse of the porous structure and further decomposition of the MOF, or, in certain situations, to the transition towards a water-stable non-porous secondary phase. As a consequence, most adsorption related applications considered for these MOFs are primarily conceptual, since the development of economical and environmentally friendly synthetic routes for intrinsically water-stable MOFs is a not yet resolved drawback [10,11].

The thermodynamic and kinetic water stability of MOFs rely on the robustness of the metal-ligand coordination bond and the hindrance of water molecules to reach the metal node, respectively [7,12]. Since the thermodynamic stability is determined by composition, the only way to modify water behavior of existing MOFs is by addressing kinetic factors affecting the reaction rate between water and the metal node. For this purpose, several post-synthetic processes have been developed to enhance the hydrophobic character of water-sensitive MOFs. These methods can be categorized into internal or external surface functionalization with hydrophobic molecules or polymers. The internal modification or functionalization of the organic linkers or metal nodes within the framework is a highly effective hydrophobization method. However, it presents the drawback of significantly reducing the MOF empty volume, which negatively affects the overall adsorption capacity [13]. Instead, the external surface coating method have demonstrated outstanding performance in preventing MOFs from water-induced degradation, while preserving the porosity to a large extent [14,15]. Similar concepts of water stability apply to bioMOFs, a subclass of MOFs involving biomolecules as the linkers, *e.g.*, biopolymers (proteins, polypeptides), monomers/macrocycles (amino acids, porphyrins, cyclodextrins), or naturally occurring edible small molecules (carbohydrates, vitamins) [16]. Based on the biocompatible character of these products, the potential of bioMOFs has been customarily developed in medical applications [17]. The use of bioMOFs in adsorption related applications, typically needing vast amounts of adsorbents, might also have economical as well as environmental benefits, since these products are built from inexpensive biomolecules through eco-friendly soft chemistry, and, besides, they are easily recyclable [18]. Following the interesting methodology previously reported [19], we have added some references as a request from one reviewer [20–26].

Taking the above points into consideration, this work explores the advantages of using hydrophobized bioMOFs in CO_2 adsorption applications [27]. The porous bioMOF CaSyr-1, recently synthesized in our laboratories following a sustainable strategy [28], is selected as a case study. Compared to other reported bioMOFs, CaSyr-1 stands out due to its unique textural properties, *i.e.*, high surface area (1080 m^2g^{-1}) and wide micropore diameter (1.4 nm), which enables the loading with molecules of different sizes [29,30]. In our previous work, CaSyr-1 demonstrated favorable CO_2 adsorption due to the affinity of this gas for both calcium nodes and methoxy groups in the linker [28]. This bioMOF presents CO_2 adsorption values as high as 3.7 mmol g^{-1} at 100 kPa and 273 K, in the range of industrially used activated carbon or zeolite 13X (*ca.* 4 mmol g^{-1}) [31]. However, CaSyr-1 would not withstand realistic conditions of industrial post-combustion gas adsorption, since it presents thermodynamic chemical instability when exposed to a humid environment and transforms into a second crystalline phase, designated as CaSyr-2. The single crystal structural analysis of this new phase, forming part of this investigation, indicates that CaSyr-2 has a non-porous 2D architecture not appropriate for adsorption related purposes. The main objective of this study is to enhance the water stability of the porous CaSyr-1 phase, thus considerably delaying its transformation to CaSyr-2 in humid environments, which would eventually allow the use of this bioMOF in CO_2 realistic adsorption applications. For this, a post-synthetic hydrophobic surface coating strategy is established by choosing stearic acid (HStear) as the modifier. HStear is a compound readily available and renewable, obtained by hydrolysis of animal fat or hydrogenation of cottonseed or vegetable oil. In a recent publication, HStear has been used to coat CaSyr-1 nanoparticles (NPs) impregnated with isoniazid, resulting in a hydrophobic nanopowder that was further processed to formulate a drug delivery system [29]. In the present work, this synthetic method is evolved to straightforwardly assembly the composite CaSyr-1/stearate (CaSyr-1/s) into a hydrophobic monolithic aerogel with multimodal porosity, in this case, intended for gas adsorption. This is an important advantage to burst scale-up production, since most MOFs are currently available as fine powders and must be transformed into useful objects, such as pellets or monoliths, before industrial application [32]. The direct use of nanopowders involves not only difficulties in handling and manipulation at operating level, but also serious concerns regarding worker's safety [33]. Besides, the assembly of MOF adsorbents into monolithic macrostructures has important advantages related to the generated meso/macroporosity as it would improve mass transfer and adsorption kinetics [34,35]. Only few examples of bare MOF monoliths have been reported [36,37]. In general, MOF NPs must be embedded in a continuous matrix, *e.g.,* graphene, silica or cellulose, to afford stable and porous monoliths [35,38]. In this research, ethanol, used for CaSyr-1/s synthesis and simultaneous assembly in a gel, and supercritical CO_2 ($scCO_2$), used for composite drying into a monolithic aerogel, are the only solvents applied during the process, thus developing an eco-friendly procedure. The behavior of CaSyr-1/s aerogel in liquid water and moisture is analyzed in regard of structure and morphology, denoting a significant enhancement of the kinetic stability with respect to the parent bioMOF. The textural and adsorption properties of the synthesized products are thoroughly investigated by using different adsorbates, including N_2, CO_2 and H_2O, at different pressures and temperatures.

2. Materials and methods

2.1. Materials

The employed reactants for CaSyr-1 and CaSyr-2 synthesis were syringic acid (H_2Syr 98%, abcr), calcium acetylacetonate ($Ca(acac)_2$ 98%, abcr), calcium chloride ($CaCl_2$ > 95%, Merck) and calcium hydroxide ($Ca(OH)_2$ > 96%, Merck). Stearic acid (HStear, Merck) was used as a surface modifier. Absolute ethanol (EtOH, Scharlab), dimethylformamide (DMF, abcr), MilliQ water (Merck Q-POD) and compressed CO_2 (CO_2 99.95 wt%, Linde Gas) were used as the solvents.

2.2. Synthetic procedure

2.2.1. Synthesis of pristine materials

CaSyr-1 was synthesized in DMF or EtOH following previously reported methods [28]. Micrometric single crystals were solvothermally (393 K, 7 days) precipitated in 25 mL of DMF by mixing 55 mg (0.50 mmol) of $CaCl_2$ and 99 mg (0.50 mmol) of H_2Syr. NPs were obtained by mixing 238 mg (1.00 mmol) of $Ca(acac)_2$ and 198 mg (1.00 mmol) of H_2Syr in EtOH at room temperature.

CaSyr-2 single crystals were straightforwardly precipitated in water. For that, 74 mg (1.00 mmol) of $Ca(OH)_2$ and 198 mg (1.00 mmol) of H_2Syr were separately dispersed in 50 mL of MilliQ water and sonicated. The suspension containing $Ca(OH)_2$ was slowly added to the H_2Syr dispersion through a filter paper to remove the small amount of non-dissolved particles (calcium carbonate traces). The addition of the basic $Ca(OH)_2$ solution induced the deprotonation of H_2Syr, which got solubilized after been softly shaken. The resulting solution was left to rest at room temperature, and single crystals, with appropriate dimensions for structural XRD elucidation using synchrotron radiation, were recovered after 24 h. The obtained product was filtered, washed thrice with MilliQ water and dried under vacuum.

2.2.2. CaSyr-1 surface modification with HStear and aerogel synthesis

A gelled suspension of CaSyr-1/s was prepared from wet CaSyr-1 NPs and HStear (Fig. 1). After a synthesis batch, CaSyr-1 was not dried following EtOH washing to avoid aggregation, that would hinder further gelation. In a 10 mL vial, a batch of wet CaSyr-1, involving *ca.* 220 mg (0.87 mmol) of CaSyr-1 according to the calculated 87 wt% yield, was redispersed in 3 mL of EtOH by vortex agitation. Separately, 284 mg (1.00 mmol) of HStear were dissolved in 4 mL of EtOH by sonication, and then added to the 10 mL vial containing the CaSyr-1 suspension. The resulting mixture was magnetically stirred (500 rpm) for *ca.* 5 min at room temperature. The stirring bar was then removed and the dispersion was allowed to stand for 10 min, resulting in the assembly of a gel (Fig. 1). Since this gel needs to be washed from HStear excess, it was transferred to a 50 mL Falcon tube and redispersed in 14 mL of fresh EtOH, thus triplicating the EtOH volume of the initial gel. The diluted dispersion was centrifuged and washed thrice with 21 mL of fresh EtOH. After supernatant elimination, the slurry was redispersed by vortex agitation in the proper EtOH volume necessary to fix the gel again (7 mL), and rapidly transferred to several small assay tubes, filling each with 1 mL. The tubes were placed into a 200 mL high-pressure vessel. Liquid CO_2 was flushed at 6 MPa and the vessel was heated at 333 K. The pressure was then increased to 20 MPa by adding CO_2 compressed with a Teledyne Isco 260D syringe pump. These working conditions were maintained for *ca.* 40 h. Finally, the reactor was isothermally depressurized and cooled down to collect the CaSyr-1/s dry aerogel monoliths (Fig. 1).

2.3. Characterization

Proton nuclear magnetic resonance (^{1}H NMR, Bruker Advance NEO 300 MHz) was used to quantify the molar ratio of Stear$^-$ with respect to Syr^{2-} in the composite CaSyr-1/s. The analysis was carried out in dimethyl sulfoxide-d$_6$ (DMSO-d$_6$; 99.5%D, abcr), after digesting the sample in hydrofluoric acid to obtain free HStear and H_2Syr [29]. The HStear signal at $\delta = 1.48$ ppm was integrated with respect to the H_2Syr signal at $\delta = 7.21$ ppm, since both signals correspond to the integration of 2H in the respective pristine organic molecules (Fig. S1-S3). Powder X-ray diffraction (XRD, Siemens D5000) patterns of the different materials were recorded at room temperature using the Cu K_α incident radiation in the 2θ range 5–30° with steps of 0.02° s^{-1}. The chemical composition of CaSyr-2 was estimated by elemental analysis (EA, Flash Smart™ elemental analyzer) and compared with the crystallographic data. The molecular arrangement was investigated using Fourier transform infrared (FTIR) spectroscopy (Jasco 4700) with attenuated total reflection (ATR) accessory. Optical (B-600 MET OPTIKA), scanning electron (SEM, Quanta FEI 200 FEG-ESEM) and transmission electron (TEM, JEOL 1210) microscopes were utilized to evaluate the morphology and size of the studied systems. The weights of main components in the composites, as well as the thermal stability, were assessed through thermogravimetric analysis in N_2 flow (TGA, SDT 650-TA instrument) by using a temperature increase step of 5 Kmin^{-1}. Ca^{2+}leaching was measured by means of a calcium electrode (Thermo Scientific Orion, Fisher Sci). A drop shape analyzer (DSA 100 KRÜSS) was used for water contact angle measurements. Isotherms of N_2, CO_2 and water adsorption-desorption were measured in samples previously activated at 393 K under vacuum during 24 h. N_2 physisorption (ASAP 2020 Micromeritics) was measured at 77 K from vacuum up to saturation pressure (101.3 kPa) and applied to characterize the porosity of the samples. The specific surface area was calculated by applying the Brunauer-Emmet-Teller (BET) equation to the recorded N_2 isotherms,

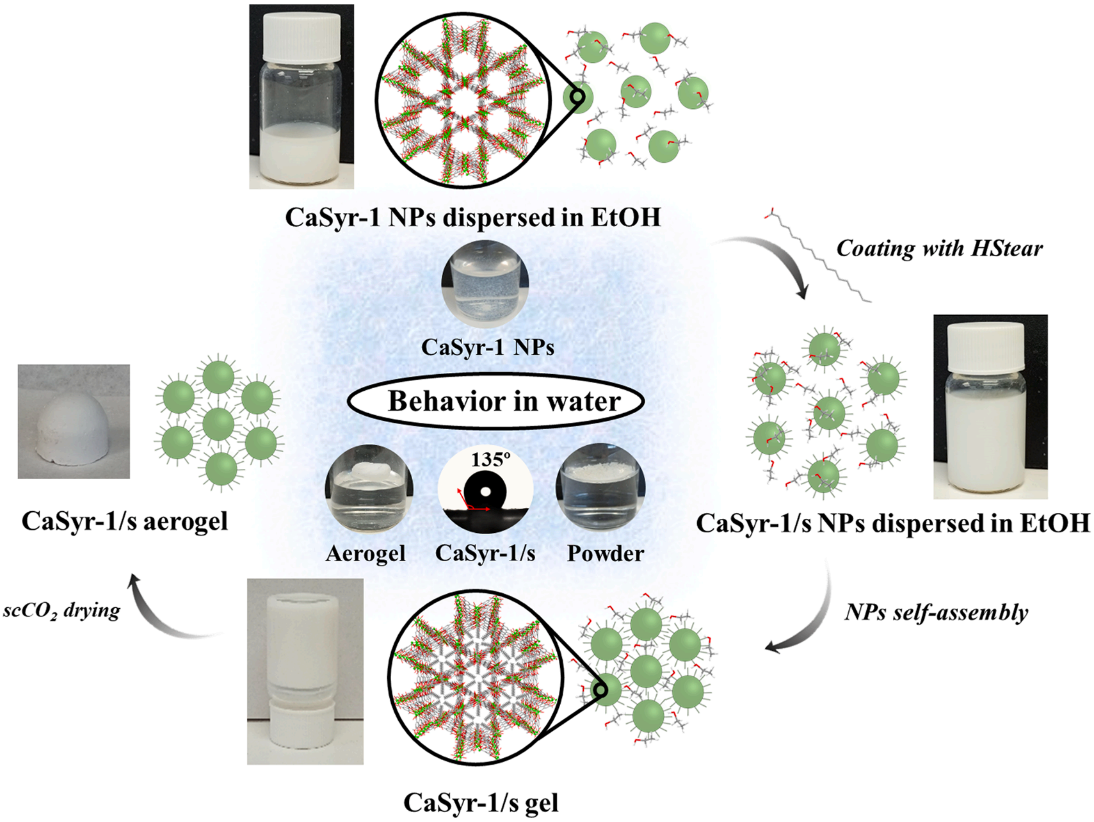

Fig. 1. Schematic representation of CaSyr-1/s aerogel synthesis including optic photographs. In the center of the figure, the behavior of CaSyr-1 NPs and CaSyr-1/s (as aerogel or grounded powder) in water is depicted, including the water contact angle of grounded CaSyr-1/s.

while the micropore volume and micropore surface area were estimated with the t-plot method. CO_2 isotherms were recorded at 273, 298 and 313 K from vacuum up to *ca.* 100 kPa using the same equipment. The CO_2 enthalpy of adsorption (Q_{st}) was determined at different levels of surface occupancy (n) by applying the Clausius-Clapeyron equation $Q_{st}(n) = -R \ln(p_2/p_1)(T_1T_2/(T_2-T_1))$. H_2O adsorption-desorption isotherms were measured at 298 K using an automatic volumetric analyzer (Belsorp MAX-II). The isotherm was recorded at different values of vapor pressure, starting from 0.037 kPa up to saturation pressure (3.17 kPa), reaching in each point the equilibrium. Each adsorption point was considered to be in equilibrium when the pressure variation was lower than 0.1% over 300 s of analysis. Single-crystal XRD experiments for the structural elucidation of CaSyr-2 were performed in the XALOC beamline at the ALBA synchrotron [39]. Data were collected at 100 K with a 0.72931 Å wavelength using a Dectris Pilatus 6 M detector placed at 120 mm from the sample. ϕ scans were performed from 0 to 360° in steps of 0.5° with a collection time of 0.15° per step. The scan was repeated at three different κ angles (0, 45 and 90°) and merged afterwards to increase the completeness and redundancy when possible. Data were indexed, integrated and scaled using the XDS software [40]. The crystal structure was solved by intrinsic phasing and refined with SHELXL (version 2014/7) [41] using Olex2 as the graphical interface [42].

3. Results and discussions

3.1. CaSyr-1 and CaSyr-2 structures and phase transition

CaSyr-1 has most of the physicochemical characteristics sought in a suitable CO_2 adsorbent. In this bioMOF, the available specific adsorption sites are conferred to the structure by functionalities found in the calcium coordination sphere, *e.g.*, coordinating H_2O molecules, and in the ligand, *e.g.*, exposed methoxy groups. Even being precipitated at the nanoscale in EtOH (*ca.* 50–70 nm, Fig. 2a), this bioMOF displays outstanding textural properties, including a large pore diameter (1.4 nm), and above average values of micropore volume (*ca.* 0.30 cm^3g^{-1}) or apparent BET surface area (1080 m^2g^{-1}). Additionally, CaSyr-1 displays a relatively high thermal stability, since the pyrolysis of its framework is not initiated up to *ca.* 600 K (Fig. S4). However, a simple trial, consisting in soaking CaSyr-1 NPs in liquid water for few minutes at room temperature, showed that added and recovered crystals had different XRD patterns (Fig. 2b). A second crystalline phase, designated here as CaSyr-2, constituted by 2D prismatic crystals of *ca.* 10–20 μm (Fig. 2a), is rapidly formed in water. The precipitated micrometric crystals displayed kink, step and terrace sites, thus indicating that CaSyr-2 grew from the dissolution of CaSyr-1.

CaSyr-1 is, thus, thermodynamically instable in contact with water, which would be detrimental for potential adsorption applications. Towards the comprehension of the irreversible CaSyr-1 to CaSyr-2 phase transition pathway in water, optical microscopy was used to *in situ* track the process, in this case starting from micrometric single crystals of CaSyr-1 synthesized in DMF. The CaSyr-1 elongated crystals (100–300 μm length), with typical hexagonal habit, were deposited on a microscope slide (Fig. 3a) to which a drop of water was added. Almost immediately, the needles of CaSyr-1 were broken laterally in small pieces due to water attack (Fig. 3b). Finally, after a few minutes, the growth of prismatic crystals of CaSyr-2 (10–20 μm) could be clearly observed (Fig. 3c).

Microscopically, the driving force for CaSyr-1 to CaSyr-2 phase transformation can be understood through the analysis of the elucidated structures by XRD synchrotron radiation. As previously reported, CaSyr-1, with elemental formula $[Ca_2(Syr)_2(H_2O)_2]_n$, belongs to the trigonal system [28]. The framework consists of interconnected dimeric units (Fig. 4a,b). The double clamp-like coordination mode of Syr^{2-} (methoxy-phenolate-methoxy) is responsible for the connection

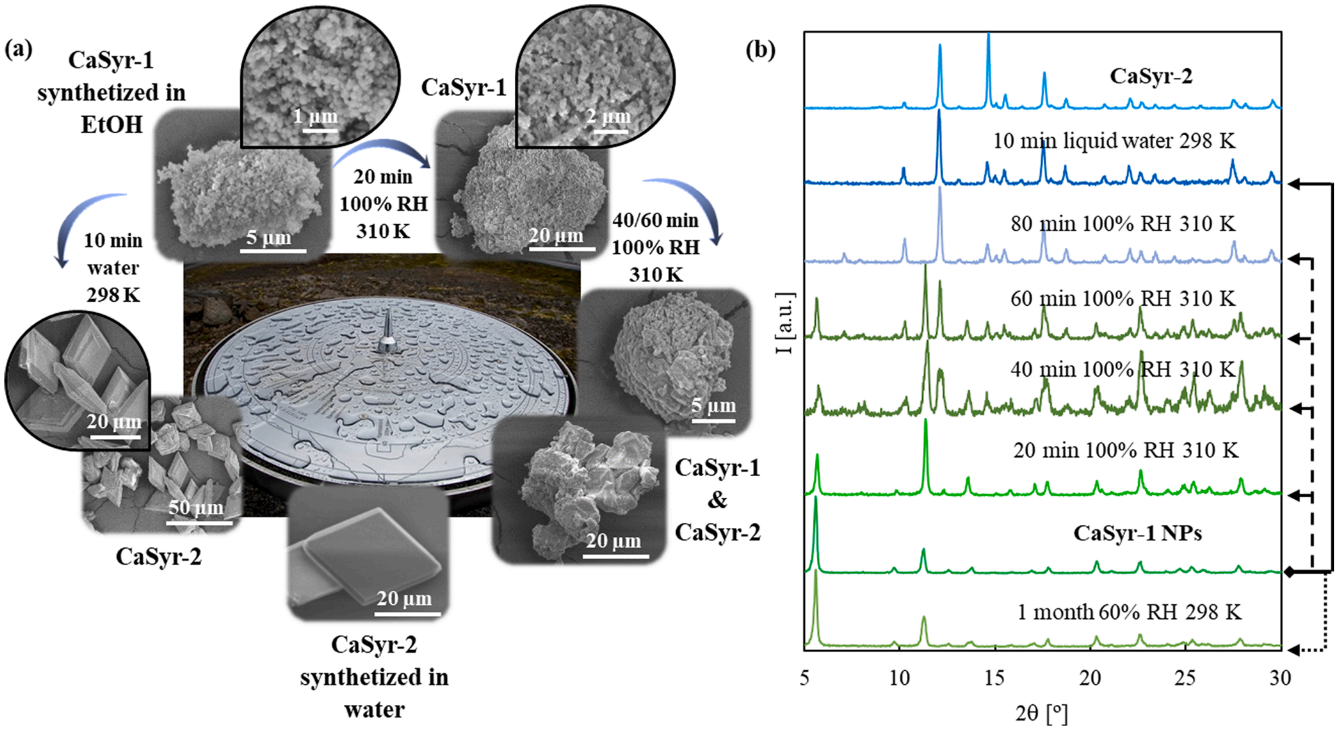

Fig. 2. Study of the transformation of CaSyr-1 to CaSyr-2: (a) SEM pictures, and (b) powder XRD patterns of CaSyr-1 NPs and CaSyr-2 micrometric crystals synthesized in EtOH and water, respectively, together with the phases obtained from the treatment of CaSyr-1 with liquid water and moisture, quantified with the relative humidity (RH) parameter, under different exposure times and temperatures. RH is defined as the percentage of H_2O vapor with respect to saturation.

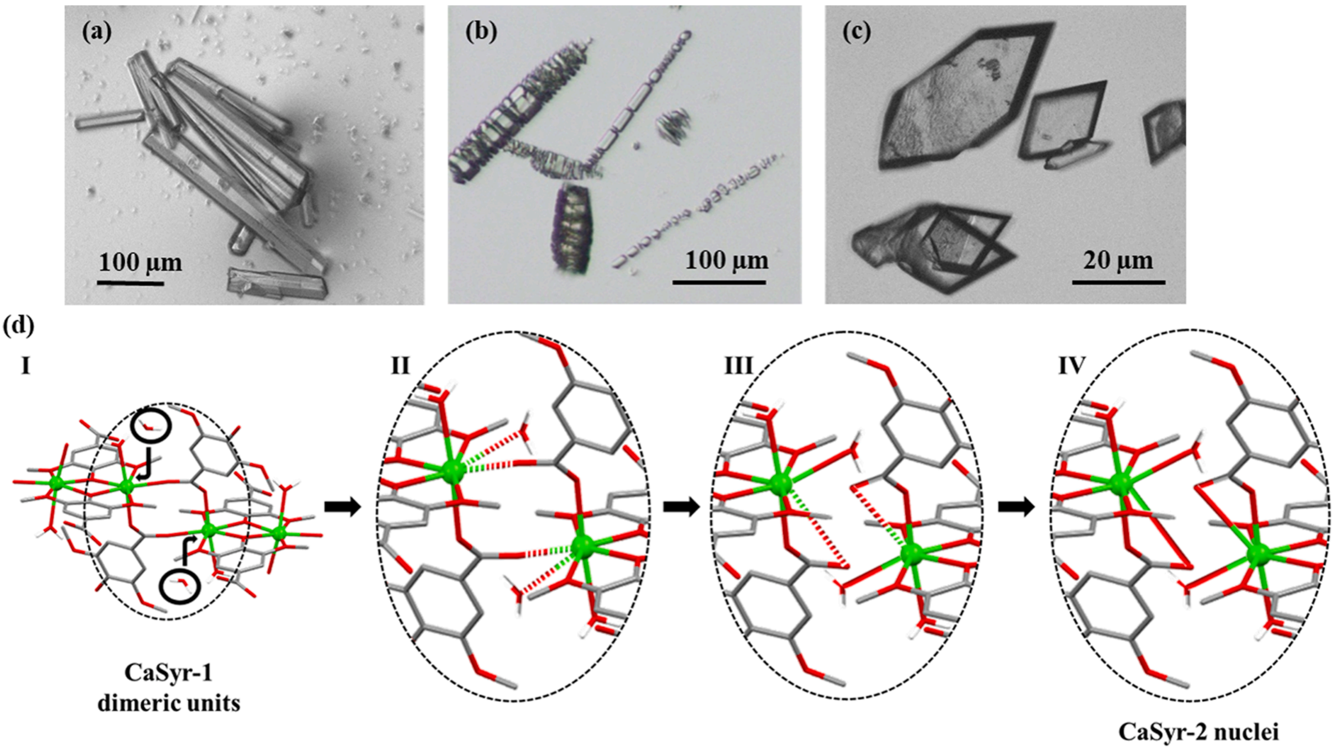

Fig. 3. Optical micrographs of: (a) CaSyr-1 crystals grown in DMF, (b) CaSyr-1 crystals after 1–2 min of water addition, and (c) CaSyr-2 crystal after 10 min of water addition; and (d) proposed mechanism for the observed phase transformation.

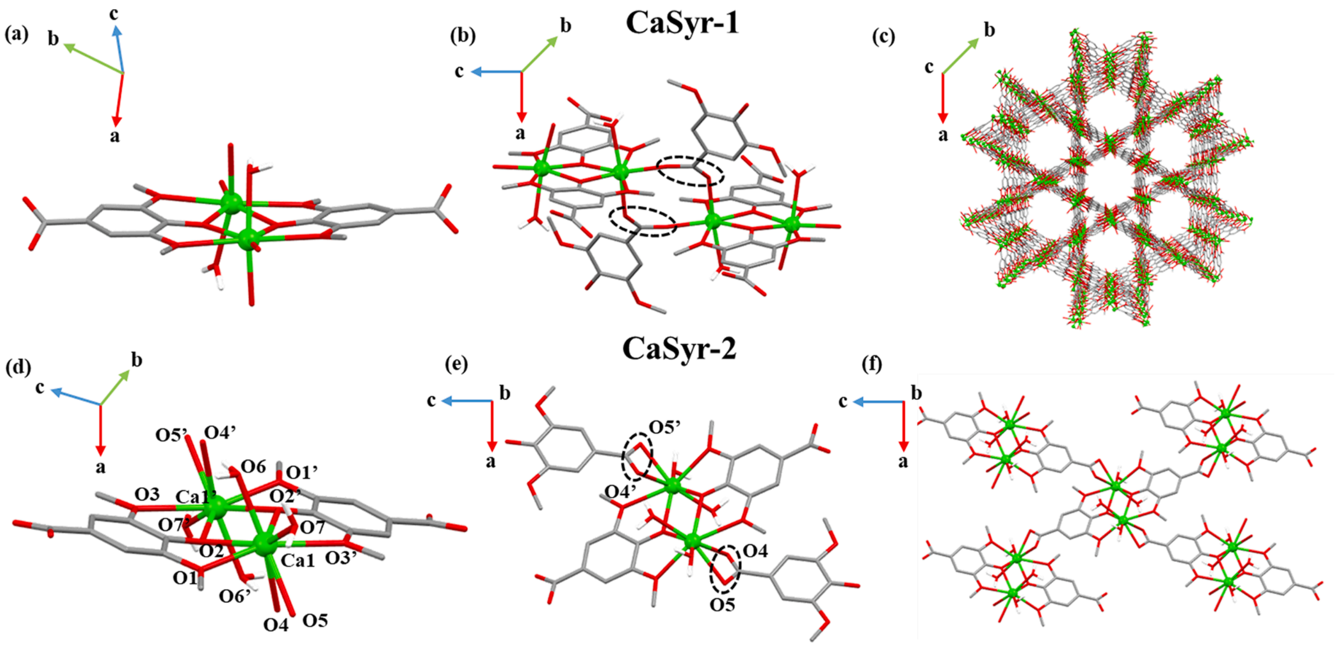

Fig. 4. Structure of: (a,b,c) CaSyr-1, being (a) the dimeric unit, (b) the dimer connection through dicarboxylate bridges, and (c) the 3D porous structure; and (d,e,f) CaSyr-2, being (d) the dimeric unit, (e) the chelating coordination mode of dicarboxylates, and (f) the dimer interconnection and extended structure.

between two Ca^{2+} and the subsequent formation of the dimer (Fig. 4a), while the syringate dicarboxylate groups serve as bridges of two different dimeric units (Fig. 4b) and promote the formation of a 3D porous framework with two types of prismatic channels, triangular and hexagonal, the latter responsible of the porosity (Fig. 4c).

CaSyr-2, structurally resolved in this work from micrometric crystals obtained in water (Fig. 2a), belongs to the orthorhombic system with the space group Pbca (Table S1). The established formula $[Ca_2(Syr)_2(H_2O)_4]_n$ agrees with elemental analysis data (Table S2), and denotes that this compound contains one additional aqua ligand per calcium cation with respect to CaSyr-1. The asymmetric unit of CaSyr-2 contains one Ca^{2+} ion, one Syr^{2-} linker and two aqua ligands, although the structure can be described considering symmetrical dimeric building units containing two Ca^{2+} ions, two Syr^{2-} linkers and four aqua ligands (Fig. 4d).

The formation of these dimers is driven by the adjacent methoxy-phenolate-methoxy groups present in Syr^{2-}, resulting in a highly stable double clamp-like coordination mode that bridges Ca1 and Ca1', similarly to CaSyr-1. Thus, the dimer core is defined by μ_2-phenoxo bridges (Ca-O2 distance 2.318(1) Å and 2.354(1) Å; Ca···Ca, 3.795(1) Å), reinforced by the concomitant coordination of each Ca^{2+} with two oxygen atoms from the methoxy groups (Ca-O1, 2450(1) Å and Ca-O3, 2.641(1) Å). The mean plane containing the oxygen atoms of the phenoxo and methoxy groups and the six carbon atoms of the aromatic ring of each linker forms an angle of 30.67(5)° with the plane defined by the Ca_2O_2 central core of the dimer. Additionally, the coordination sphere of each calcium includes two aqua ligands and two oxygen atoms (O4 and O5) from a nearly symmetrical chelate (μ^1-η^2) carboxylate group of a close neighbor dimer (Fig. 4e), which is slightly tilted in comparison with the aromatic ring of the syringate ligand (15.30(6)°). Therefore, calcium shows a coordination number eight with a roughly square antiprismatic geometry [43]. Each dimeric unit is connected to four adjacent units (Fig. 4f), defining 2D layers that are parallel to the *ac* plane (Fig. 5a). Although isolated CaSyr-2 layers seem to include some empty space, the voids get completely blocked upon hydrogen bonding-mediated inter-layer stacking (Fig. 5b), resulting in a non-porous 3D supramolecular architecture (Fig. 5c), as confirmed by N_2 adsorption-desorption analysis (Fig. S5). This absence of porosity contrasts with the high void volume of the closely related CaSyr-1. The key aspect that dictates these differences resides in the coordination mode of the carboxylate groups of the syringate, acting as a bridge between dimeric units in CaSyr-1 (Fig. 4b) and as a chelate in CaSyr-2 (Fig. 4e). Hence, whereas each Syr^{2-} in CaSyr-1 interconnects three dimeric subunits (one through the double clamp phenoxo, and two through the asymmetric μ^2-η^1: η^1 carboxylate bridge), in the CaSyr-2 structure Syr^{2-} only interconnects two units (one through the double clamp phenoxo and another by the chelating carboxylate).

On the basis of the structural singularity of each phase, the mechanism of phase transformation in water, schematized in Fig. 3d, is rationalized as starting with aqua molecules approaching the bimetallic centers of CaSyr-1 (I), in a way that each one interacts with one calcium and promotes the substitution of the Ca-O(carboxylate) bond by a Ca-OH_2 bond (II), thus starting the dissolution process. Next, the released pendant oxygen can interact with a calcium atom from the neighboring dimer, where the other oxygen from the carboxylate is linked (III), thus resulting in syringate chelated carboxylate groups (IV). CaSyr-2 nuclei are thus formed by the lateral disconnection among CaSyr-1 dimers, as observed at the macroscopic scale (Fig. 3b). The process continues until CaSyr-2 crystallizes at expenses of CaSyr-1 dissolution.

CaSyr-1 to CaSyr-2 phase transformation occurs not only when the former is immersed in water, but also when this phase is exposed to an atmosphere of high moisture content. This behavior was observed by subjecting CaSyr-1 NPs to and atmosphere of 100% RH at 310 K in a closed recipient. Phase evolution was monitored by analyzing the structure and morphology of the sample at intervals of 20 min. XRD patterns denoted that both phases, CaSyr-1 and CaSyr-2, were present after 40 min, and phase transition was completed after 80 min (Fig. 2b). Contrarily, the onset of CaSyr-1 dissolution can be already observed by SEM in pictures taken after 20 min, which displayed an even surface for the NPs (Fig. 2a), although this transformation was not still reflected in the XRD pattern. At 40 and 60 min, the observed aggregates were a mixture of decomposing CaSyr-1 NPs and growing micrometric crystals of CaSyr-2. Nevertheless, CaSyr-1 has a considerable kinetic stability under ambient conditions (60% RH at 298 K). According to XRD analysis, CaSyr-1 was stable when stored under these conditions for at least one month (Fig. 2b).

3.2. *CaSyr-1/s aerogel*

Even the kinetic stability of CaSyr-1 is demonstrated to be significant under ambient conditions, this bioMOF would transform to CaSyr-2 in most of the humid industrial environments applied for gas adsorption. Hence, for this target application, water stability of CaSyr-1 must be increased, but compulsorily maintaining the internal pore volume available for adsorption. A process of selective hydrophobic functionalization of the external surface of the bioMOF NPs is designed in this study for this purpose. It is reasoned that external selective

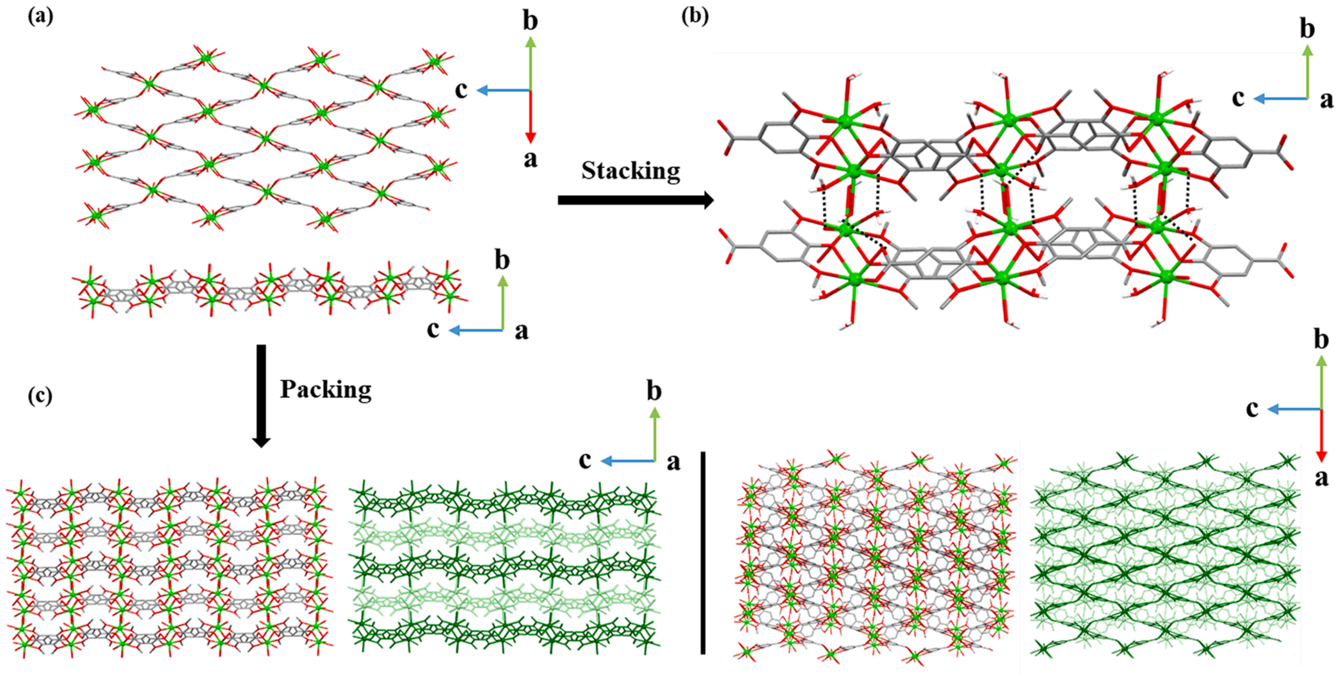

Fig. 5. Structure of CaSyr-2: (a) extended 2D, (b) stacking of the layers through hydrogen bonding, and (c) packing (the two green tones represent not coordinated layers).

functionalization could be achieved by using a bulky coating agent, which, due to size-exclusion would not enter the CaSyr-1 cavities. However, it is worth mentioning that due to the large diameter of the pores in CaSyr-1, complete exclusion from the pores would be difficult to achieve. After evaluating several candidates, stearic acid was selected as an optimal modifier, since this natural organic acid is endowed with a long aliphatic tail imparting a large hydrophobic character, and a carboxylic polar head with high affinity for calcium. Moreover, it is cheap, abundant and renewable, and can be processed *via* a sustainable approach based exclusively on the use of EtOH as a solvent. This coating agent has previously proved to be effective in increasing the hydrophobicity of several MOFs [29,44–46]. However, this mostly occurs at the cost of blocking the pores in the framework, which disqualified the system for further adsorption applications. This negative feature is circumvented in this study by properly setting the reaction and activation conditions.

In this study, it was experimentally observed that, by adding stearic acid to CaSyr-1 NPs dispersed in EtOH, a non-flowing gel-like product was suddenly formed (Fig. 1). The gelation process is envisaged to occur in two steps: first, the suspended NPs are coated with HStear, mainly reacting with the crystallographic defects present on the NPs surface, and, second, gelation is driven by the hydrophobic interactions between the solvent-exposed aliphatic domains in the different NPs. The CaSyr-1/s gel is then dried using scCO$_2$ to obtain a highly porous aerogel [47]. In this method, the EtOH solvent of the gel is mixed with added scCO$_2$ under mild conditions of pressure and temperature (20 MPa and 333 K, respectively). The EtOH/CO$_2$ mixture is eliminated from the solid under supercritical conditions to overcome the development of capillary forces, thus avoiding the collapse of the meso/macroporous network of the gel. The recovered product is a dry aerogel monolith of CaSyr-1/s (Fig. 1). Unlike net CaSyr-1 NPs, which rapidly transformed into CaSyr-2 when immersed into water (Fig. 1), the CaSyr-1/s aerogel floated on the surface of the liquid phase when added either as one-piece or grounded into powder (Fig. 1). The liquid phase was analyzed for leaching of calcium ions, indicating negligible values of dissolved cation, which points to null dissolution of CaSyr-1 bioMOF. The hydrophobic behavior of the composite aerogel was corroborated by measuring the water contact angle in a compacted aerogel, giving a value of *ca.* 135° (Fig. 1), characteristic of a water-repellent material. Hydrophobicity is conferred to the block by the aliphatic domains of stearate anions oriented towards the exterior of CaSyr-1 NPs.

^{1}H NMR was used to ascertain the content of stearate with respect to CaSyr-1, providing a ratio of *ca.* 0.4 mol of stearate per mol of CaSyr-1, calculated from the empirical formula of the MOF (Fig. S1-S3). Regarding the composite structure, CaSyr-1/s displayed all the XRD peaks observed for net CaSyr-1, and a wide incipient extra signal at $2\theta =$ 21–22°, which can be attributed to the formation of a small fraction of calcium stearate or stearic acid impurities (Fig. 6), both phases presenting intense diffraction peaks at these angles [48,49]. In the ATR-FTIR spectrum of CaSyr-1/s, most of the observed bands match those of pristine CaSyr-1 signals and are assigned to the skeleton of syringate (Fig. S6). The presence of stearate is assessed by the increase of the C–H symmetric and asymmetric stretching bands at 2920–2850 cm^{-1}. C═O stretching, typically emerging as an intense signal for free stearic acid at *ca.* 1700 cm^{-1}, shifted to lower wavenumber values in stearate coating, denoting deprotonation and coordination with calcium [50]. TGA data indicated that CaSyr-1/s aerogel and the parent CaSyr-1 NPs have similar thermal stability (Fig. S4). Essentially, the stablished carboxylate bonds of the Ca-syringate and Ca-stearate types must be of similar energy, both breaking above 600 K. The significant weight loss observed for CaSyr-1 at *ca.* 400 K was attributed to the evaporation of traces of solvent and adsorbed water, phenomenon that was clearly reduced for the hydrophobic bioMOF. Slight differences could be noticed in the region between 450 and 530 K, assigned to the pyrolysis of organic acids, where the functionalized CaSyr-1/s aerogel experienced a decay of *ca.* 2 wt%, not present for pristine CaSyr-1. This indicates that small amounts of free HStear might be adsorbed in the structure. SEM images indicated similar appearance for CaSyr-1 NPs in the pristine bioMOF (Fig. S7a) and in the composite aerogel (Fig. S7b). However, in the aerogel, the NPs were organized in a macroporous network, while the pristine NPs formed dense aggregates. TEM images revealed that the size of the CaSyr-1 NPs in both CaSyr-1 and CaSyr-1/s samples were comparable (Fig. S7c,d). However, the NPs in CaSyr-1/s exhibited less defined surfaces compared to the parent material, likely due to the dynamic nature of the stearate aliphatic tails [29].

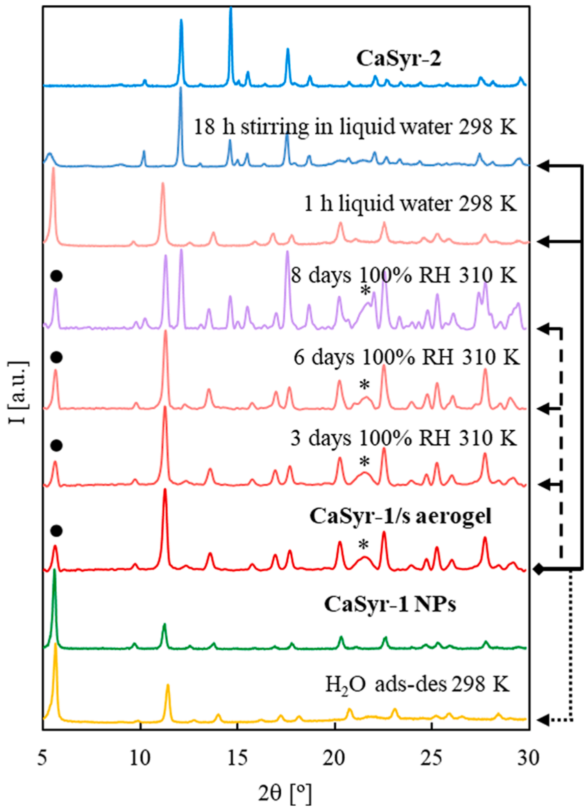

Fig. 6. Powder XRD patterns of CaSyr-1 NPs, CaSyr-1/s aerogel and CaSyr-2 microcrystals, and CaSyr-1/s behavior when exposed to water, either liquid at 298 K (solid line) or moisture at 100% RH and 310 K (dashed line) or after a cycle of water vapor adsorption-desorption at 298 K (dotted line). Asterisks (*) indicate the broad signal at $2\theta =$ 21–22° associated with free stearic acid, observed for the CaSyr-1/s aerogel sample prior to pore activation by using either vapor or liquid water. Black dots (●) mark the CaSyr-1 peak at $2\theta =$ 5.7°, with reduced intensity (respect to empty pore samples) due to the presence of free stearic acid into the pores of CaSyr-1/s aerogel.

The effect of the post-synthetic modification with stearate on the phase transition of CaSyr-1 to CaSyr-2 was evaluated in liquid water at 298 K and in a humid environment at 310 K. First, the grounded CaSyr-1/s aerogel was placed in contact with liquid water for 1 h at 298 K. Under these conditions, CaSyr-1/s particles were not wet by the liquid phase and remained floating on the interphase water-air. No significant differences could be spotted in the SEM images (Fig. S7e) or in the XRD pattern (Fig. 6) of the recovered sample in comparison to the initial CaSyr-1/s aerogel, with just some variations in the relative intensity of the XRD peaks, indicating that phase transition did not take place. However, when stirring the pulverized CaSyr-1/s monolith in water for several hours, the recorded XRD pattern pointed to its complete transformation to CaSyr-2 (Fig. 6), which indicates that the coated sample was not thermodynamically stable in water. Exposure to liquid water induces the cleavage of Ca-Stear bonds and the progressive release of HStear, which forms crystals with a characteristic flake-like morphology (Fig. S7f). Conversely, during tests conducted at 100% RH and 310 K, the CaSyr-1 framework in CaSyr-1/s aerogel remained stable up to one week, as evidenced by the XRD analysis (Fig. 6), time after which peaks corresponding to CaSyr-2 emerged in the diffraction pattern. These findings demonstrate that the post-synthetic modification of CaSyr-1 with stearate results in a remarkable enhancement of the kinetic stability of the framework against water, reflected in the time frame that goes from minutes in the pristine bioMOF to several days in the aerogel. After one week of water exposure, the CaSyr-2 phase progressively forms, eventually becoming the predominant component of the material. At this stage, the non-porous nature of CaSyr-2 would limit the suitability of this material for adsorption applications.

3.3. *Adsorption*

Low temperature N_2 physisorption at different relative pressures (p/p^0, where p^0 is the saturation pressure) was used to determine the textural properties of the composite and constituent NPs. Net CaSyr-1 displayed a type I isotherm at low p/p° corresponding to intraparticle micropores, developing hysteresis at medium-high p/p^0, related to interparticle mesoporosity, corresponding to type IV isotherm (Fig. S5). A value of apparent BET surface area of 1080 m^{2}g^{-1} was calculated from the isotherm, which includes a micropore surface area of *ca.* 900 m^{2}g^{-1}. The specific external surface area can then be approximated to 180 m^{2}g^{-1}. This value, together with the measured specific relative amount of stearate in the composite (1.6·10^{-3} mol g$^{-1}_{CaSyr-1}$), and estimating the surface area occupied by one mol of stearate on *ca.* 4.3 × 10^8 cm^{2}mol^{-1} (stearate molecular size taken as *ca.* 0.3 × 2.4 nm diameter x length), allow evaluating the percentage of coated external surface area, giving *ca.* 70 m^{2}g^{-1}. This value corresponds to *ca.* 40% of potential total coverage, assuming all stearate heads are anchored on the outer surface of the NPs at these conditions, *i.e.*, 77 K. Actually, this is a notable high percentage of surface covering, which can be attained on account of the large degree of dispersion of the CaSyr-1 NPs when structured in an aerogel. Comparing to pristine CaSyr-1, CaSyr-1/s offers singular textural properties originated by the particular arrangement of the NPs in the aerogel-like macrostructure (Fig. S7b). Thus, the recorded isotherm for CaSyr-1/s starts with type II at low p/p^0, not displaying the microporosity intrinsically provided to the system by CaSyr-1. Next, an H3 hysteresis cycle from a type IV isotherm, associated to grove voids generated by NPs aggregation, is observed at medium-high p/p^0 (Fig. S5). The isotherm did not exhibit a saturation limit, indicating indefinite multi-layer formation. This is a behavior characteristic of aerogels constituted by particles containing *meso* and macropores with a wide distribution of pore size. The measured BET surface area has a value of 70 m^{2}g^{-1}. The lack of N_2 physisorption in the micropores of the composite is ascribed to hindered access of gas molecules to the internal cavities of the bioMOF caused by functionalization with stearate and concomitant steric hindrance. Pore entrance blocking is exacerbated by the almost null mobility of the aliphatic chains at the low temperature used for the analysis, corresponding to that of liquid N_2 (77 K). Based on that argument, it was reasoned that an increase in the analysis temperature, for instance to room temperature, would enhance gas adsorption by conferring substantial dynamic mobility to the aliphatic domains of the coating agent. Since N_2 adsorption at room temperature is very poor due to its negligible polarity, the adsorption of CO_2, with a significant quadrupole moment, was chosen to perform new measurements at 298 K. CO_2 has been widely employed to study ultramicropores [51], thus, it is expected for the molecules of the gas to pass through the small openings statistically occasioned by the dynamics of the aliphatic tails. At saturation pressure and 298 K, CaSyr-1/s aerogel adsorbed *ca.* 16 cm^{3}g$^{-1}_{CaSyr-1/s}$ of CO_2 (or 23 cm^{3}g$^{-1}_{CaSyr-1}$ when recalculated with respect to the weight of CaSyr-1 exclusively) (Fig. 7a). Nevertheless, this amount is only half of that adsorbed by pristine CaSyr-1 (or 49 cm^{3}g$^{-1}_{CaSyr-1}$) under similar conditions. Minimizing at 298 K the influence of steric barriers that limit the uptake into the internal pore volume, partial occupancy of micropore volume by stearic acid was considered to explain the observed behavior. Actually, the cylindrical HStear molecule, with a geometrical diameter of *ca.* 0.3 nm, could penetrate the 1.4 nm channels of CaSyr-1, even the dynamic disorder of the tails would enlarge its effective diameter (Fig. 8a). The insertion of HStear in the porous system is possibly driven through hydrogen bonding with the exposed coordinating H_2O molecules of the calcium sphere, easily reachable in the hexagonal channels of CaSyr-1. As previously anticipated in the TGA analysis (Fig. S4), small amounts of free HStear could be found in the structure, which, due to cumulative steric impedance, should be most likely adsorbed on the inner walls of the pores close to the entrance, thus resulting in partial blocking of the bioMOF empty pore for further CO_2 adsorption (Fig. 8b).

To further analyze the water stability of the hydrophobized aerogel, as well as the water uptake into the hydrophilic CaSyr-1 component, the adsorption-desorption isotherm of H_2O at 298 K and different relative pressures was measured for CaSyr-1/s and compared with that of pristine CaSyr-1 (Fig. 7b). Water adsorption was chosen because it has been used to study ultra-small micropores in hydrophilic compounds owing to

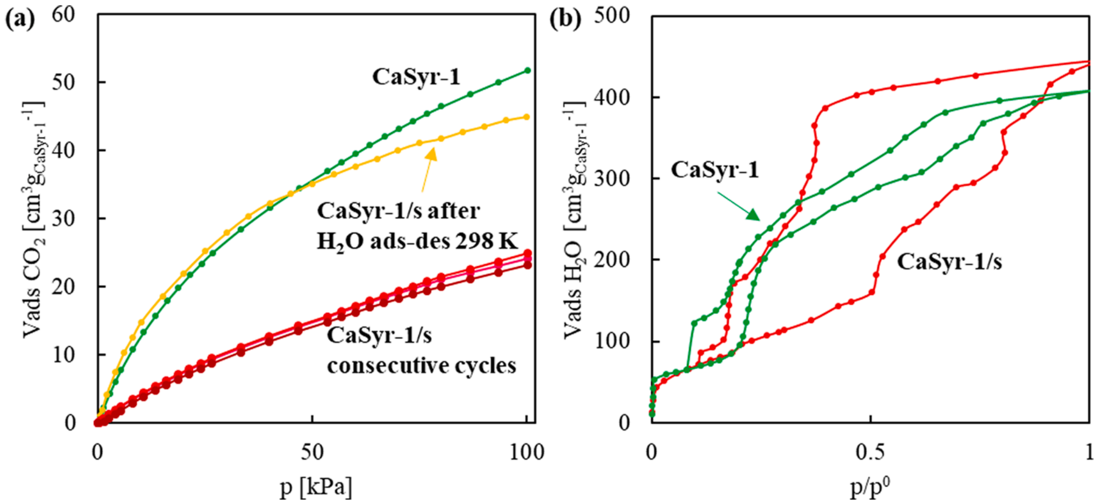

Fig. 7. Adsorption behavior of the studied materials: (a) CO_2 adsorption isotherms at 298 K for net CaSyr-1 NPs (green), CaSyr-1/s aerogel in three consecutive cycles (reddish tones), and CaSyr-1/s aerogel after a cycle of vapor H_2O adsorption-desorption at 298 K (yellow), and (b) H_2O adsorption-desorption isotherms at 298 K for CaSyr-1 NPs (green) and CaSyr-1/s aerogel (red), in both graphs considering only the mass of CaSyr-1 in the sample to calculate the volumetric specific adsorption.

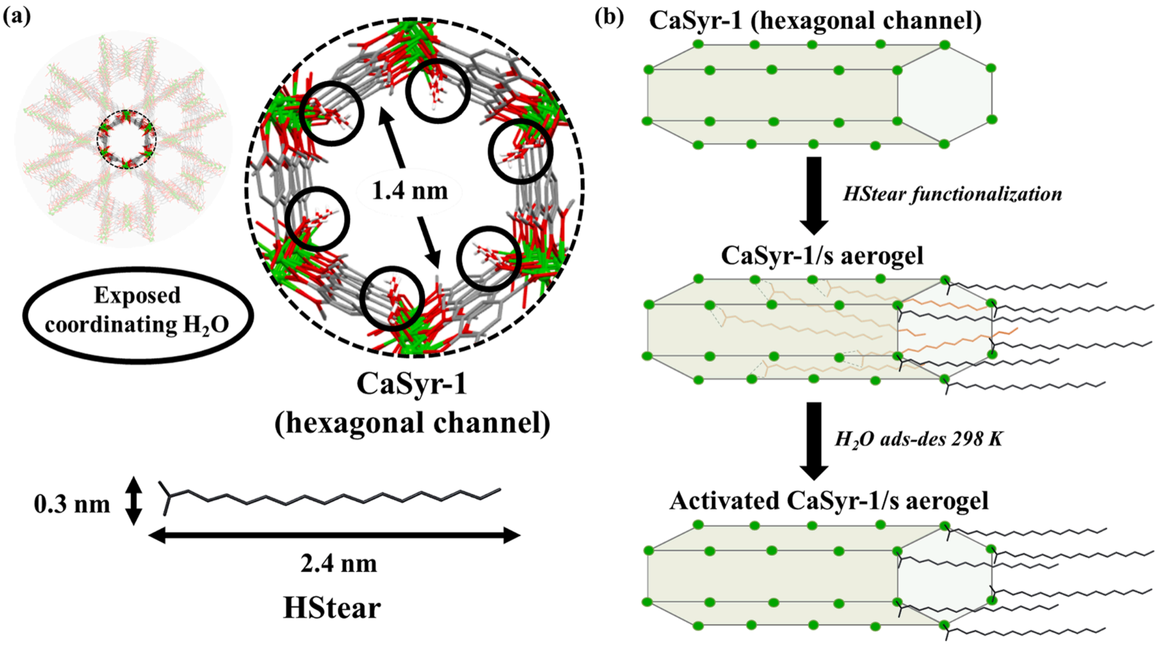

Fig. 8. CaSyr-1 functionalization and activation with water: (a) hexagonal channels of CaSyr-1, indicating pore diameter and the exposed coordinating H_2O molecules, as well as dimensions of Hstear, (b) schematic representation of HStear functionalization on CaSyr-1 and subsequent activation with H_2O vapor at 298 K (HStear adsorbed through hydrogen bonding at the walls in the inner cavities and chemisorbed on the external surface, in orange and black, respectively).

H_2O small molecular diameter [52]. Notably, CaSyr-1/s exhibited an extraordinary water uptake at 298 K and saturation pressure, in the order of 340 $cm^3 g^{-1}_{CaSyr\text{-}1/s}$ (or 450 $cm^3 g^{-1}_{CaSyr\text{-}1}$), close to values reported for hydrophilic MOFs designed for this application [53]. Compared to pristine CaSyr-1, CaSyr-1/s required higher p/p^0 to take up significant amounts of H_2O, as the adsorption process was hindered by the presence of hydrophobic stearate molecules on the bioMOF external surface. However, by increasing water vapor pressure, discrete H_2O molecules could progressively penetrate the hydrophobic coating and reach the hydrophilic CaSyr-1 micropores, ultimately resulting in a higher H_2O uptake than for bare CaSyr-1 (410 $cm^3 g^{-1}_{CaSyr\text{-}1}$). The lower adsorption value observed for pristine CaSyr-1 with respect to CaSyr-1/s is related to the onset of water-induced framework degradation. Differences between the two samples were also evident by studying the desorption branch. While desorption in CaSyr-1 closely follows the adsorption pathway, indicating similar activation energy for both processes, water desorption in CaSyr-1/s was significantly less favorable than adsorption, leading to a type IV isotherm with H2 hysteresis. This hysteresis curve is associated with ink bottle shaped pores, with smaller diameter at the entrance than in the main channel. In the particular case of CaSyr-1/s, the pore opening diameter is reduced by stearate coating. Additionally, the desorption process involves water leaving the hydrophilic pores of CaSyr-1 through the adverse hydrophobic environment formed on the outer surface of the particles. XRD characterization of the treated sample indicated that the framework of CaSyr-1 did not suffer any structural change during water adsorption/desorption (Fig. 6). Interestingly, the pattern of CaSyr-1/s sample collected after this process recovered the ratio of relative intensities for the most intense peaks observed for pristine CaSyr-1, which was modified in the as-synthesized CaSyr-1/s sample. Similar changes could be noted in the CaSyr-1/s sample treated with liquid water at 298 K for 1 h. Main differences between CaSyr-1 and as-synthesized CaSyr-1/s were found analyzing the intensity of the low angle peak arisen at $2\theta = 5.7^\circ$, which was indexed to the (2–10) reflection. This signal is assigned in the CaSyr-1 crystal to the ordered arrangement of the micropores. For net CaSyr-1, this is an intense and sharp diffraction peak indicating empty pores, attained after sample activation. This peak is still present in the as-synthesized aerogel, but with lower relative intensity than in net CaSyr-1. The reduction in intensity of low-angle peaks in nanoporous compounds has been described as an indication of reversible deformation of pore walls when they are loaded with guest molecules [54], which in the case of CaSyr-1/s, can only be HStear. In the XRD pattern of the sample recovered after water adsorption/desorption, the low angle peak is again a sharp signal of high intensity, thus suggesting the activation of the micropores.

With the objective of verifying sample activation through water adsorption, the sample recovered after the water adsorption/desorption experiment was subjected to second cycles of N_2 and CO_2 adsorption at 77 and 298 K, respectively. Again, the adsorption of N_2 at low pressures was negligible, as it was for the as-synthesized CaSyr-1/s, which confirms that for this gas the main effect hindering adsorption in the micropores is pore entrance blocking by frozen aliphatic chains with null mobility at 77 K (Fig. S5). Instead, CO_2 adsorption at room temperature in the water-activated sample was enhanced by a factor of two with respect to the vacuum-activated sample, reaching and uptake of 31 $cm^3 g^{-1}_{CaSyr\text{-}1/s}$ (or 45 $cm^3 g^{-1}_{CaSyr\text{-}1}$), which means that *ca.* 92 v% of the net CaSyr-1 empty volume for CO_2 adsorption was recovered (Fig. 7a). A plausible explanation for the enhanced CaSyr-1 activation attained with water is the displacement of the HStear impregnated in the pores (Fig. 8b). Previous studies have shown that when saturated vapor is inside micropores, the adsorbed fluid density increases to near-liquid water due to the high influence of the wall interactions [55]. In this particular case, this liquid water behavior could interfere in the hydrogen bonding interactions formed between HStear and the coordinating H_2O molecules, thus resulting in the replacement of HStear by an extended H-bonded water network inside the pores, which would further push the aliphatic compound to the outer surface. These results suggest that CaSyr-1 to CaSyr-2 conversion might be initiated in the external surface of the MOF, as the presence of near-liquid water in the pores does not induce this phase transformation. Activation with CO_2 was not attained in the as-synthesized sample studied in this work, not even after three consecutive CO_2 adsorption-desorption cycles at 298 K (Fig. 7a), denoting that it does not interfere in the supramolecular interactions of the adsorbed HStear with the walls of the pores.

A fundamental parameter to evaluate the advantages of an adsorbent for a particular adsorbate is the isosteric enthalpy of adsorption (Q_{st}), measured at different levels of surface occupancy [56]. For CaSyr-1 and CaSyr-1/s, measured Q_{st} values were near constant at the different gas loadings (Fig. S8), with values of 16–18 and 31–34 J mmol^{-1}, respectively. Even all quantities were in the range of physisorption, the CO_2 adsorption enthalpy was notably higher for the CaSyr-1/s aerogel than for net CaSyr-1. Found differences are related to the activation method used in each case, thermal activation under vacuum for CaSyr-1 and water vapor activation for CaSyr-1/s. Regarding the integrity of the CaSyr-1 framework, water vapor activation can be considered as a more aggressive method than thermal activation. The water treatment is prone to induce surface defects on the pore walls, resulting in increased Q_{st} values. Nevertheless, this increment, far from being an inconvenient, suggests that CaSyr-1/s would have an enhanced affinity for CO_2. The generation of defects in the crystalline structure of MOFs have proved to increase their adsorption performance for specific gases [57].

4. Conclusions

This study illustrates an efficient method to produce water-stable frameworks starting from moisture-sensitive MOFs. In the designed protocol only green solvents, *i.e.*, EtOH, for MOF coating and simultaneous assembly in a gel, and $scCO_2$, for composite drying into a monolithic aerogel, and a readily available organic acid, *i.e.*, stearic acid, are used throughout the post-synthetic modification of the MOF, thus involving a sustainable and cost-effective strategy. The protocol enables the surface hydrophobization of MOF NPs with stearate and the simultaneous spontaneous self-assembly of the functionalized particles into an interconnected aerogel-like macrostructure, which supposes advantages from an operational perspective, but also in regard of the intrinsic characteristics of the material. This study is focused on CaSyr-1 bioMOF, but the proposed functionalization could also be extended to other water-sensitive MOFs containing metals with affinity to carboxylic acids, thus representing a novel general strategy to accomplish both surface hydrophobization and NPs 3D macrostructuration. Stearate coating significantly increases the kinetic stability of CaSyr-1 against moisture, thus avoiding its rapid transformation into the non-porous CaSyr-2 phase. Indeed, high values of H_2O vapor adsorption could be attained in the CaSyr-1/s aerogel without affecting the structural integrity of the framework. Furthermore, this H_2O adsorption-desorption process benefits the adsorptive capacities of CaSyr-1/s by activating the material through the displacement of impregnated HStear inside the pores. CO_2 adsorption at room temperature in the water-activated sample was enhanced by a factor of two with respect to the vacuum-activated sample, reaching and uptake of 31 cm^{3}g$^{-1}_{\mathrm{CaSyr\text{-}1/s}}$ (45 cm^{3}g$^{-1}_{\mathrm{CaSyr\text{-}1}}$). The resulting activated CaSyr-1/s aerogel exhibits CO_2 uptake values comparable with the ones for net CaSyr-1, in which *ca.* 92 v% of the net CaSyr-1 empty volume for CO_2 adsorption was recovered. In short, the resulting activated CaSyr-1/s aerogel exhibits CO_2 uptake values comparable with the ones observed for net CaSyr-1, denoting that the proposed hydrophobic coating can benefit the kinetic stability of the MOF while preserving the intrinsic adsorption characteristics of the material, as long as the activation protocol follows a water vapor treatment before vacuum. The stability of CaSyr-1/s structure and adsorption performance under long-term humidity exposure and multiple CO_2/H_2O adsorption-desorption cycles needs to be analyzed in a future work to ensure the application of this modified bioMOF in more realistic conditions.

CRediT authorship contribution statement

Albert Rosado: Writing – original draft, Visualization, Methodology, Investigation, Formal analysis, Data curation, Conceptualization. **Alejandro Borrás:** Software, Formal analysis, Data curation. **Fabián Suárez-García:** Software, Resources, Formal analysis, Data curation. **Oriol Vallcorba:** Software, Resources, Formal analysis, Data curation. **Ana M. López-Periago:** Writing – review & editing, Supervision, Resources, Project administration, Funding acquisition, Conceptualization. **José A. Ayllón:** Writing – review & editing, Supervision, Resources, Project administration, Methodology, Funding acquisition, Conceptualization. **Concepción Domingo:** Writing – review & editing, Visualization, Supervision, Resources, Project administration, Investigation, Funding acquisition, Conceptualization.

Declaration of competing interest

The authors declare that they have no known competing financial interests or personal relationships that could have appeared to influence the work reported in this paper.

Acknowledgments

This work was supported by the Spanish Ministry of Science and Innovation through the Severo Ochoa Program for Centers of Excellence (CEX2023–001263-S), the Spanish National Plan of Research with project PID2020-115631GB-I00 and Ecological Transition and Digital Transition Project TED2021-1298378-C41. This work has been performed in the framework of the doctoral program “Chemistry” of the UAB by A.R. that acknowledges the financial support of an FPI 2019 grant. We acknowledge the thorough language and text revision performed by Rosy Sunday.

Supplementary materials

Supplementary material associated with this article can be found, in the online version, at doi:10.1016/j.apmt.2024.102573.

Data availability

Data will be made available on request. CCDC 2298353 (Original data).

References

[1] H.-C. Zhou, J.R. Long, O.M. Yaghi, Introduction to metal–organic frameworks, Chem. Rev. 112 (2012) 673–674.

[2] Z. Chen, S.L. Hanna, L.R. Redfern, D. Alezi, T. Islamoglu, O.K. Farha, Reticular chemistry in the rational synthesis of functional zirconium cluster-based MOFs, Coord. Chem. Rev. 386 (2019) 32–49.

[3] S.T. Meek, J.A. Greathouse, M.D. Allendorf, Metal-organic frameworks: a rapidly growing class of versatile nanoporous materials, Adv. Mater. 23 (2011) 249–267.

[4] C. Petit, Present and future of MOF research in the field of adsorption and molecular separation, Curr. Opin. Chem. Eng. 20 (2018) 132–142.

[5] N.C. Burtch, H. Jasuja, K.S. Walton, Water stability and adsorption in metal–organic frameworks, Chem. Rev. 114 (2014) 10575–10612.

[6] Y. Chen, J. Ma, H. Yang, H. Ji, W. Li, Y. Pi, H. Pang, Application of modified metal-organic frameworks in water treatment, Mater. Today Chem. 30 (2023) 101577.

[7] C. Wang, X. Liu, N.K. Demir, J.P. Chen, K. Li, Applications of water stable metal–organic frameworks, Chem. Soc. Rev. 45 (2016) 5107–5134.

[8] P.A. Julien, C. Mottillo, T. Friščić, Metal–organic frameworks meet scalable and sustainable synthesis, Green Chem. 19 (2017) 2729–2747.

[9] S. Yuan, L. Feng, K. Wang, J. Pang, M. Bosch, C. Lollar, Y. Sun, J. Qin, X. Yang, P. Zhang, Q. Wang, L. Zou, Y. Zhang, L. Zhang, Y. Fang, J. Li, H.-C. Zhou, Stable metal–organic frameworks: design, synthesis, and applications, Adv. Mater. 30 (2018) 1704303.

[10] L. Wang, X. Li, B. Yang, K. Xiao, H. Duan, H. Zhao, The chemical stability of metal-organic frameworks in water treatments: fundamentals, effect of water matrix and judging methods, Chem. Eng. J. 450 (2022) 138215.

[11] M. Rubio-Martinez, C. Avci-Camur, A.W. Thornton, I. Imaz, D. Maspoch, M.R. Hill, New synthetic routes towards MOF production at scale, Chem. Soc. Rev. 46 (2017) 3453–3480.

[12] Y. An, X. Lv, W. Jiang, L. Wang, Y. Shi, X. Hang, H. Pang, The stability of MOFs in aqueous solutions—Research progress and prospects, Green Chem. Eng. 5 (2024) 187–204.

[13] B. Liu, K. Vikrant, K.-H. Kim, V. Kumar, S.K. Kailasa, Critical role of water stability in metal–organic frameworks and advanced modification strategies for the extension of their applicability, Environ. Sci. Nano 7 (2020) 1319–1347.

[14] M. Ding, X. Cai, H.-L. Jiang, Improving MOF stability: approaches and applications, Chem. Sci. 10 (2019) 10209–10230.

[15] X. Shi, G. Annie, S. Liu, D. Kim, A. Alahmed, A. Jamal, L. Wang, A-H.A. Park, Water-stable MOFs and hydrophobically encapsulated MOFs for CO$_2$ capture from ambient air and wet flue gas, Mater. Today 65 (2023) 207–226.

[16] A. Shahzaib, Shaily, L.A. Kamran, N. Nishat, The Biomolecule-MOF Nexus: recent advancements in biometal-organic frameworks (Bio-MOFs) and their multifaceted applications, Mater. Today Chem. 34 (2023) 101781.

[17] S. Rojas, T. Devic, P. Horcajada, Metal organic frameworks based on bioactive components, J. Mater. Chem. B 5 (2017) 2560–2573.

[18] T. Li, D.-L. Chen, J.E. Sullivan, M.T. Kozlowski, J.K. Johnson, N.L. Rosi, Systematic modulation and enhancement of CO$_2$:N$_2$ selectivity and water stability in an isoreticular series of bio-MOF-11 analogues, Chem. Sci. 4 (2013) 1746–1755.

[19] F.-X. Yang, Y.-F. Zhu, S. Cao, C.-M. Wang, Y.-J. Ma, R. Yang, Q.-M. Hu, Origin of the distinct site occupations of H atom in hcp Ti and Zr/Hf, Int. J. Hydrogen Energy 91 (2024) 933–941.

[20] G.H. Al-Hazmi, L.A. Albedair, R.A.S. Alatawi, A.M. Alsuhaibani, A.A.H. Bukhari, A. A. El-Bindary, Effective synthesis and characterization of citric acid cross-linking of modified ferrous metal-organic framework and chitosan nanocomposite sponge for Th(IV) elimination: adsorption isotherms, kinetic analysis, and optimization by Box-Behnken design, Int. J. Bio. Macromolec. 281 (2024) 136194.

[21] H.M. Nassef, G.A.A.M. Al-Hazmi, A.A. Alayyafi, M.G. El-Desouky, A.A. El-Bindary, Synthesis and characterization of new composite sponge combining of metal-organic framework and chitosan for the elimination of Pb(II), Cu(II) and Cd(II) ions from aqueous solutions: batch adsorption and optimization using Box-Behnken design, J. Mol. Liq. 394 (2024) 123741.

[22] A.M. Alsuhaibani, A.A.A. Alayyafi, L.A. Albedair, M.G. El-Desouky, A.A. El-Bindary, Synthesis and characterization of metal–organic frameworks based on thorium for the effective removal of 2,4-dichlorophenylacetic pesticide from water: batch adsorption and Box-Behnken Design optimization, and evaluation of reusability, J. Mol. Liq. 398 (2024) 124252.

[23] M.G. El-Desouky, A.A.A. Alayyafi, G.A.A.M. Al-Hazmi, A.A. El-Bindary, Effect of metal organic framework alginate aerogel composite sponge on adsorption of tartrazine from aqueous solutions: adsorption models, thermodynamics and optimization via Box-Behnken design, J. Mol. Liq. 399 (2024) 124392.

[24] A.M. Alsuhaibani, A.A.A. Alayyafi, L.A. Albedair, M.G. El-Desouky, A.A. El-Bindary, Efficient fabrication of a composite sponge for Cr(VI) removal via citric acid cross-linking of metal-organic framework and chitosan: adsorption isotherm, kinetic studies, and optimization using Box-Behnken design, Mater. Today Sust. 26 (2024) 100732.

[25] A. Almahri, M. Morad, M.M. Aljohani, N.M. Alatawi, F.A. Saad, H.M. Abumelha, M. G. El-Desouky, A.A. El-Bindary, Atrazine reclamation from an aqueous environment using a ruthenium-based metal-organic framework, Process Saf. Env. Prot. 177 (2023) 52–68.

[26] N.A.H. Alshammari, J.S. Alnawmasi, A.M. Alotaibi, O.A.O. Alshammari, M. A. Abomuti, N.H. Elsayed, A.A. El-Bindary, Efficient adsorption of fluorescein dye from aqueous solutions by Al/Th-MOF bimetal-organic frameworks: adsorption isotherm, kinetics, DFT computation, and optimization via Box-Behnken design, Process Saf. Env. Prot. 190 (2024) 353–371.

[27] A. Zulys, F. Yulia, N. Muhadzib, N. Nasruddin, Biological metal−organic frameworks (Bio-MOFs) for CO$_2$ capture, Ind. Eng. Chem. Res. 60 (2021) 37–51.

[28] A. Rosado, O. Vallcorba, B. Vázquez-Lasa, L. García-Fernández, R.A. Ramírez-Jiménez, M.R. Aguilar, A.M. López-Periago, C. Domingo, J.A. Ayllón, Facile, fast and green synthesis of a highly porous calcium-syringate bioMOF with intriguing triple bioactivity, Inorg. Chem. Front. 10 (2023) 2165–2173.

[29] A. Rosado, L. García-Fernández, M.R. Aguilar, R.A. Ramírez, A.M. López-Periago, J.A. Ayllón, C. Domingo, Supercritical CO$_2$ assisted bioMOF drug encapsulation and functionalization for delivery with a synergetic therapeutic value, J. Supercrit. Fluids 216 (2025) 106452.

[30] A. Rosado, A. Borrás, M. Sánchez-Soto, M. Labíková, H. Hettegger, R.A. Ramírez-Jiménez, L. Rojo, L. García-Fernández, M.R. Aguilar, F. Liebner, A.M. López-Periago, J.A. Ayllón, C. Domingo, BioMOF@cellulose glycerogel scaffold with multifold bioactivity: perspective in bone tissue repair, Gels 10 (2024) 631.

[31] L. Hauchhum, P. Mahanta, Carbon dioxide adsorption on zeolites and activated carbon by pressure swing adsorption in a fixed bed, Int. J. Energy Environ. Eng. 5 (2014) 349–356.

[32] Q. Ma, T. Zhang, B. Wang, Shaping of metal-organic frameworks, a critical step toward industrial applications, Matter 5 (2022) 1070–1091.

[33] S. Seal, B. Karn, Safety aspects of nanotechnology based activity, Saf. Sci. 63 (2014) 217–225.

[34] J. Hou, A.F. Sapnika, T.D. Bennett, Metal–organic framework gels and monoliths, Chem. Sci. 11 (2020) 310–323.

[35] A. Rosado, A. Borrás, J. Fraile, J.A.R. Navarro, F. Suárez-García, K.C. Stylianou, A. M. López-Periago, J. Giner Planas, C. Domingo, A. Yazdi, HKUST-1 metal–organic framework nanoparticle/graphene oxide nanocomposite aerogels for CO$_2$ and CH$_4$ adsorption and separation, ACS Appl. Nano Mater. 4 (2021) 12712–12725.

[36] M.R. Lohe, M. Rose, S. Kaskel, Metal–organic framework (MOF) aerogels with high micro- and macroporosity, Chem. Commun. (2009) 6056–6058.

[37] B. Bueken, N. Van Velthoven, T. Willhammar, T. Stassin, I. Stassen, D.A. Keen, G. V. Baron, J.F.M. Denayer, R. Ameloot, S. Bals, D. De Vos, T.D. Bennett, Gel-based morphological design of zirconium metal–organic frameworks, Chem. Sci. 8 (2017) 3939–3948.

[38] L. Wang, H. X, J. Gao, J. Yao, Q. Zhang, Recent progress in metal-organic frameworks-based hydrogels and aerogels and their applications, Coord. Chem. Rev. 398 (2019) 213016.

[39] J. Juanhuix, F. Gil-Ortiz, G. Cuní, C. Colldelram, J. Nicolás, J. Lidón, E. Boter, C. Ruget, S. Ferrera, J. Benacha, Developments in optics and performance at BL13-XALOC, the macromolecular crystallography beamline at the Alba Synchrotron, J. Synchrotron Radiat. 21 (2014) 679–689.

[40] W. Kabsch, XDS, Acta Crystallogr. D Biol. Crystallogr. 66 (2010) 125–132.

[41] G.M. Sheldricka, Crystal structure refinement with SHELXL, Acta Crystallogr. A Found. Crystallogr. 71 (2015) 3–8.

[42] O.V. Dolomanov, L.J. Bourhis, R.J. Gildea, J.A.K. Howard, H. Puschmann, OLEX2: a complete structure solution, refinement and analysis program, J. Appl. Crystallogr. 42 (2009) 339–341.

[43] A.K. Katz, J.P. Glusker, S.A. Beebe, C.W. Bock, Calcium ion coordination: a comparison with that of beryllium, magnesium, and zinc, J. Am. Chem. Soc. 118 (1996) 5752–5763.

[44] M. Huang, J. Zhang, X. Ke, S. Gao, D. Wu, J. Chen, Y. Weng, Stearic acid modified nano CuMOFs used as a nitric oxide carrier for prolonged nitric oxide release, RSC Adv. 12 (2022) 2383–2390.

[45] J. Zhang, X. Pei, J. Huang, X. Ke, C. Xu, W. Zhao, L. Li, Y. Weng, J. Chen, Construction of hierarchical micro/nanostructured ZnO/Cu–ZnMOFs@SA superhydrophobic composite coatings with excellent multifunctionality of anticorrosion, Blood-Repelling, and Antimicrobial Properties, ACS Appl. Mater. Interfaces 15 (2023) 265–280.

[46] J. Zhang, X. Pei, Y. Liu, X. Ke, Y. Peng, Y. Weng, Q. Zhang, J. Chen, Combining chitosan, stearic acid, and (Cu-, Zn-) MOFs to prepare robust superhydrophobic coatings with biomedical multifunctionalities, Adv. Healthcare Mater. 12 (2023) 2300746.

[47] A.M. López-Periago, C. Domingo, Features of supercritical CO$_2$ in the delicate world of the nanopores, J. Supercrit. Fluids 134 (2018) 204–213.

[48] M. Goto, E. Asada, The crystal structure of the B-form of stearic acid, Bull. Chem. Soc. Jpn. 51 (1978) 2456–2459.

[49] M. Gonen, S. Ozturk, D. Balkose, S. Okur, S. Ulku, Preparation and characterization of calcium stearate powders and films prepared by precipitation and Langmuir-Blodgett techniques, Ind. Eng. Chem. Res. 49 (2010) 1732–1736.

[50] K. Saito, T. Xu, H.J. Ishikita, Correlation between C=O stretching vibrational frequency and pKa shift of carboxylic acids, J. Phys. Chem. B 126 (2022) 4999–5006.

[51] A.S. Palakkal, R.S. Pillai, Tuning the ultra-micropore size of fluorinated MOFs (M′F6-Ni-L) for CO$_2$ capture from flue gases by advanced computational methods, J. Phys. Chem. C 124 (2020) 16975–16989.

[52] M.R. Tchalala, Y. Belmabkhout, K. Adil, K.N. Chappanda, A. Cadiau, P.M. Bhatt, K. N. Salama, M. Eddaoudi, Concurrent sensing of CO$_2$ and H$_2$O from air using ultramicroporous fluorinated metal-organic frameworks: effect of transduction mechanism on the sensing performance, ACS Appl. Mater. Interfaces 11 (2019) 1706–1712.

[53] B. Zhang, Z. Zhu, X. Wang, X. Liu, F. Kapteijn, Water adsorption in MOFs: structures and applications, Adv. Funct. Mater. 34 (2023) 2304788.

[54] G.A. Zickler, Jähnert S, W. Wagermaier, S.S. Funari, G.H. Findenegg, O. Paris, Physisorbed films in periodic mesoporous silica studied by *in situ* synchrotron small-angle diffraction, Phys. Rev. B 73 (2006) 184109.

[55] A. Giaya, R.W. Thompson, Water confined in cylindrical micropores, J. Chem. Phys. 117 (2002) 3464–3475.

[56] A. Torres-Knoop, A. Poursaeidesfahani, T.J.H. Vlugt, D. Dubbeldam, Behavior of the enthalpy of adsorption in nanoporous materials close to saturation conditions, J. Chem. Theory Comput. 13 (2017) 3326–3339.

[57] S. Li, W. Han, Q.F. An, K.T. Yong, M.J. Yin, Defect engineering of MOF-based membrane for gas separation, Adv. Funct. Mater. 33 (2023) 2303447.